

Two-integral Schwarzschild models

E.K. Verolme^{*} and P.T. de Zeeuw

Leiden Observatory, Postbus 9513, 2300 RA Leiden, The Netherlands

Accepted 0000 0000. Received 0000 0000; in original form 0000 0000

ABSTRACT

We describe a practical method for constructing axisymmetric two-integral galaxy models (with distribution functions of the form $f(E, L_z)$, in which E is the orbital energy, and L_z is the vertical component of the angular momentum), based on Schwarzschild's orbit superposition method. Other $f(E, L_z)$ -methods are mostly based on solving the Jeans equations or on finding the distribution function directly from the density, which often places restrictions on the shape of the galaxy. Here, no assumptions are made and any axisymmetric density distribution is possible. The observables are calculated (semi-)analytically, so that our method is faster than most previous, fully numerical implementations. Various aspects are tested extensively, the results of which apply directly to three-integral Schwarzschild methods. We show that a given distribution function can be reproduced with high accuracy and investigate the behaviour of the parameter that is used to measure the goodness-of-fit. Furthermore, we show that the method correctly identifies the range of cusp slopes for which axisymmetric two-integral models with a central black hole do not exist.

Key words: galaxies: elliptical and lenticular, cD - galaxies: kinematics and dynamics - galaxies: structure

1 INTRODUCTION

The fundamental quantity in galaxy dynamics is the distribution function (DF), which specifies the distribution of the stars in a galaxy over position and velocity. By Jeans' theorem, the DF is a function of the isolating integrals that are conserved by the corresponding potential (e.g., Lynden-Bell 1962; Binney 1982). Axisymmetric galaxies, which we will study here, conserve at least the two classical integrals of motion, the energy E and the vertical component of the angular momentum L_z . The DF can generally not be measured directly, but since observationally accessible quantities, such as the projected density and the line-of-sight velocity, are simple moments of the DF, photometric and kinematic observations can provide information on its properties. In some cases, the part of a two-integral distribution function that is even in the velocities, $f(E, L_z^2)$, can be obtained analytically by using integral transforms to solve the relation between the DF and the intrinsic density $\rho(R, z)$, where (R, ϕ, z) are the usual cylindrical coordinates. The odd part can be found similarly from $\rho(v_\phi)$, where $\langle v_\phi \rangle$ is the mean streaming velocity. These Laplace (Lynden-Bell 1962; Lake 1981), Stieltjes (Hunter 1975b) and Laplace-Mellin (Dejonghe 1986) transforms have the drawback that

numerical implementation is difficult and that they require ρ and v_ϕ to be explicit functions of the potential V and the cylindrical radius R . A more general formalism (Hunter & Qian 1993; Qian et al. 1995, hereafter Q95), the HQ-method, uses contour integration instead of integral transforms. This means it is simpler to implement, does not explicitly require $\rho(R, V)$ and $v_\phi(R, V)$, but a suitable contour for the integration has to be chosen, which may not always be at hand.

Because of the drawbacks of these analytical formalisms, numerical methods that can be applied to arbitrary potential-density pairs are more attractive. Various methods have been developed, many of which circumvent knowledge of the DF by solving the Jeans equations directly (van der Marel et al. 1994; Magorrian 1995), while others assume that the DF can be represented by a superposition of basis functions (Dehnen & Gerhard 1994; Kuijken 1995). Accurate estimates of the mass-to-light ratio M/L can be obtained in both ways (van der Marel 1991; Shaw et al. 1993; van den Bosch 1996). The predicted central black hole masses that are obtained with two-integral models (Magorrian et al. 1998) seem to overestimate the true values, but are still very useful to narrow down the parameter range for more sophisticated modeling (van der Marel et al. 1998, hereafter vdM98; Gebhardt et al. 2000; Bower et al. 2001).

Numerical orbit integrations and observations of, e.g., the anisotropy of the stellar dispersions in the solar neighbourhood show that, in addition to E and L_z , a third inte-

^{*} verolme@strw.leidenuniv.nl

gral is conserved for most orbits. In separable potentials, this third integral is exact and has a closed form (e.g., Kuzmin 1956; de Zeeuw 1985), allowing a direct calculation of the DF (e.g., Dejonghe & de Zeeuw 1988). The most general family of these potentials corresponds to flattened mass models with constant-density cores (de Zeeuw, Franx & Peletier 1986), which provide a poor description of the inner regions of most galaxies, since these contain a central density cusp (Lauer et al. 1995). We conclude that many of the existing two-integral, as well as the analytical three-integral methods, are applicable to a limited range of galaxy models.

A flexible method for calculating numerical galaxy models was designed by Schwarzschild (1979, 1982), who represented the DF numerically by the occupation numbers in a superposition of building blocks. There are no restrictions on the density or the potential, and no a priori assumptions have to be made about the shape or the degree of anisotropy of the galaxy. Schwarzschild's original implementation was aimed at reproducing a given triaxial density distribution and was subsequently applied to a large variety of galaxy models, from spherically and axially symmetric (Richstone & Tremaine 1984; Levison & Richstone 1985) to triaxial density distributions (e.g., Vietri 1986; Statler 1987; Schwarzschild 1993, Merritt & Friedman 1996; Siopis & Kandrup 2000). More general versions of the method can also reproduce kinematical observations of spherically and axially symmetric galaxies that obey up to three integrals of motion (Zhao 1996; Rix et al. 1997, hereafter R97; Cretton et al. 1999, hereafter C99; Cretton et al. 2000; Häfner et al. 2000).

In most implementations of Schwarzschild's method, orbits are used as individual building blocks. In non-separable potentials the third integral of motion is not known explicitly, so that the orbital properties can only be obtained by solving the equations of motion numerically. This orbit integration has to be carried out until the relevant quantities have averaged out and do not change upon a new time-step (Pfenniger 1984; Copin et al. 2000). Especially for orbits that are near-stochastic, or that have nearly commensurate fundamental frequencies, this condition is difficult to achieve and the orbit integration can be very time-consuming. Furthermore, an orbit fills a region in space that can have sharp edges, depending on the combination of integrals of motion that it obeys. A superposition of a finite (and relatively small) number of orbits can therefore show artefacts that are caused by these edges. One way to solve this is to 'blur' orbits in phase-space randomly, another is to use building blocks that are smoother (e.g., Zhao 1996; Merritt & Friedman 1996; R97; C99). Of particular interest are the so-called isotropic and two-integral components (ICs and TICs). Isotropic components, which are completely specified by their energy E , fill the volume inside the equipotential at E , while TICs, which are fixed once E and L_z are chosen, completely fill the corresponding zero-velocity curve (ZVC). The advantages of these building blocks is apparent: both the equipotential and the ZVC are smooth surfaces, and ICs and TICs can be considered as weighted combinations of all orbits with the same energy E (or E and L_z), including the irregular orbits.

These building blocks can be used in Schwarzschild's method in two ways. They can be added to every energy or every combination (E, L_z) of a (three-integral) orbit library, which will 'automatically' take care of the stochastic orbits

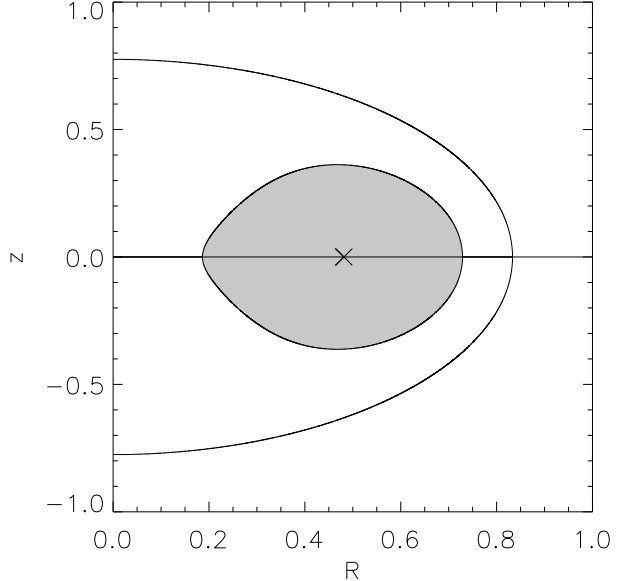


Figure 1. The meridional-plane cross section of the toroidal volume defined by the energy E and angular momentum L_z in an axisymmetric potential. Its boundary is the zero-velocity curve ZVC. When $L_z = 0$, the ZVC coincides with the equipotential (indicated by the drawn curve), and the hole around the z -axis disappears. When the angular momentum is maximal, the ZVC reduces to the circular orbit (indicated by the cross).

(Zhao 1996; R97; C99). Alternatively, a fully isotropic or two-integral model can be constructed by using only ICs or TICs as building blocks. C99 suggested that this might be a practical way of constructing such models, and derived some analytic properties, but did not pursue these models further. We do so in this paper and concentrate on the two-integral case, since the properties of the isotropic components follow from those of the TICs by taking $L_z = 0$.

In §2, we collect the properties of the TICS, and summarize how we use them in Schwarzschild's method. The numerical aspects are discussed in detail in §3. We show in §4 that our method can reproduce a model with a known analytical distribution function with high accuracy. We also study a set of mass models with a central black hole, and show that our method is able to detect when a self-consistent solution does not exist. We summarize our conclusions in §5. Applications of our software to model the observed two-dimensional surface brightness and kinematics of nearby elliptical galaxies observed with **SAURON** and **STIS** are described in two follow-up papers (Verolme et al. 2002, in preparation; McDermid et al. 2002, in preparation).

2 TWO-INTEGRAL COMPONENTS

We introduce the two-integral components (TICs) and calculate their observable properties, and then describe how we use them to construct two-integral models for galaxies. The properties of ICs follow by taking $L_z = 0$.

2.1 Properties

A TIC is completely specified by its energy E_j and angular momentum $L_{z,j}$ (where j is a label for the TIC) and is defined by its distribution function

$$f_{[E_j, L_{z,j}]} = \begin{cases} C \delta(E - E_j) \delta(L_z - L_{z,j}) & \text{inside ZVC,} \\ 0 & \text{elsewhere,} \end{cases} \quad (1)$$

with C a constant that is used to normalize the mass of the TIC. The abbreviation ZVC denotes the zero-velocity curve in the (R, z) -plane, defined as the locus of points for which

$$E_{\text{kin}} = V_{\text{eff}}(R, z) - E = 0, \quad (2)$$

where

$$V_{\text{eff}}(R, z) = V(R, z) - \frac{L_z^2}{2R^2}, \quad (3)$$

is the effective potential. The ZVC defines a toroidal volume around the z -axis (Fig. 1) with inner and outer radii R_1 and R_2 . The size of the central hole is determined by the value of the angular momentum: when $L_z = 0$, there is no hole at all ($R_1 = 0$) and the torus fills the equipotential at the given energy completely, so that the TIC reduces to the isotropic component (IC) at that energy. For the maximum value $L_z = R_c v_c$ (with $v_c^2 = R_c \partial V_{\text{eff}}(R_c)/\partial R_c$ the circular velocity at radius R_c) the torus reduces to the circular orbit at E_j , and $R_1 = R_2 = R_c$.

The density $\rho_j(R, z)$ of a TIC is defined as the integral of the DF over all velocities, and is given by

$$\rho_j(R, z) = \begin{cases} \frac{\pi C}{R} & \text{inside ZVC,} \\ 0 & \text{elsewhere.} \end{cases} \quad (4)$$

The velocity moments are defined as the average of (powers of) the velocity components over all velocities. From symmetry arguments and from the fact that $f = f(E, L_z)$, the only nonzero first and second moments are

$$\begin{aligned} \langle v_\phi \rangle &= \frac{\pi C L_{z,j}}{R^2} \\ \langle v_\phi^2 \rangle &= \frac{\pi C L_{z,j}^2}{R^3} \\ \langle v_R^2 \rangle &= \langle v_z^2 \rangle = \frac{\pi C}{R} [V_{\text{eff}}(R, z) - E_j], \end{aligned} \quad (5)$$

where these expressions are valid inside the ZVC. All moments vanish outside the ZVC.

We assume that the galaxy is observed at an inclination i , so that the projected coordinates are given by

$$\begin{aligned} x' &= y \\ y' &= -x \cos i + z \sin i \\ z' &= x \sin i + z \cos i, \end{aligned} \quad (6)$$

where x' and y' are chosen in the plane of the sky, with y' along the projected minor axis of the galaxy, and z' is measured along the line of sight.

The projected density $\Sigma_j(x', y')$ is the integral of the intrinsic density along the line of sight

$$\Sigma_j(x', y') = \int \frac{\pi C dz'}{\sqrt{x'^2 + (z' \sin i - y' \cos i)^2}}, \quad (7)$$

which can be evaluated analytically. The intrinsic density of a TIC is only defined for points that lie inside the toroidal

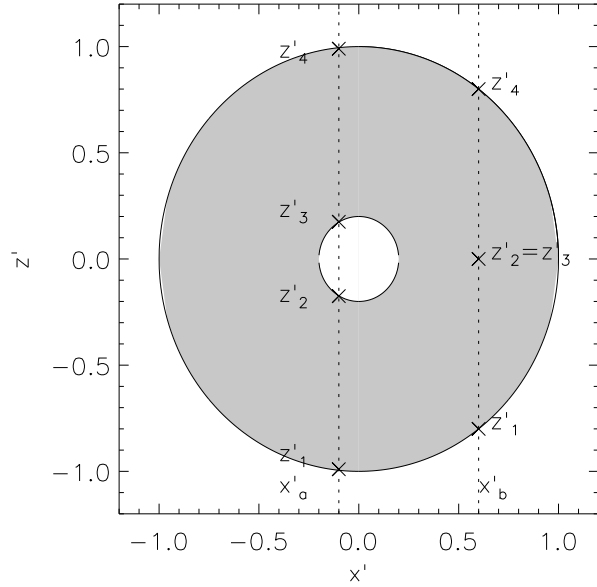


Figure 2. The line-of-sight crosses the ZVC in two (case b) or four (case a) points, depending on the location of (x', y') . The plot shows an edge-on configuration, so that the intersections are pairwise symmetric.

volume defined by the ZVC, so that the integral (7) is defined on the z' -intervals delimited by the two or four points where the line-of-sight crosses the ZVC (Fig. 2). We give all expressions for four intersections, labeled as $z'_1 < z'_2 \leq 0 \leq z'_3 < z'_4$. The case of two intersections follows by taking $z'_2 = z'_3 = 0$. We obtain

$$\Sigma_j(x', y') = \Sigma_{z'_4} - \Sigma_{z'_3} + \Sigma_{z'_2} - \Sigma_{z'_1}, \quad (8)$$

with

$$\Sigma_{z'_k} = \frac{\pi C}{\sin i} \ln \left[2 \sin i \left(R_{z'_k} + D_{z'_k} \right) \right], \quad k = 1, \dots, 4, \quad (9)$$

where we have defined

$$R'_{z'} = \sqrt{x'^2 + (z' \sin i - y' \cos i)^2} \quad (10)$$

and

$$D_{z'} = z' \sin i - y' \cos i. \quad (11)$$

The limiting case of edge-on viewing ($i = 0$) is given by

$$\Sigma_{z'_k} = \frac{\pi C z'_k}{\sqrt{x'^2 + y'^2}}, \quad k = 1, \dots, 4, \quad (12)$$

The velocity profile $\mathcal{L}_j(x', y', v_{z'})$, defined as the distribution of stars over velocity $v_{z'}$ at the position (x', y') , is the integral of $f(E, L_z)$ over the line of sight and the two velocity components $v_{x'}$ and $v_{y'}$ in the plane of the sky. Since the distribution function of a TIC is the product of two δ -functions, the triple integral in the expression for \mathcal{L}_j reduces to a single integral,

$$\mathcal{L}_j(x', y', v_{z'}) = C \int dz' J_{E_j L_{z,j}}, \quad (13)$$

where the remaining integration in z' is over the same intervals as in eq. (7), and $J_{E_j L_{z,j}}$ is the Jacobian for the change of variables from $(v_{x'}, v_{y'})$ to $(E_j, L_{z,j})$. It can be written as (C99)

$$J_{E_j L_{z,j}} = \frac{1}{\sqrt{A + B v_{z'} + C v_{z'}^2}}, \quad (14)$$

with

$$\begin{aligned} A &= 2 [V(x', y', z') - E_j] (x'^2 \cos^2 i + D_{z'}^2) - L_{z,j}^2, \\ B &= -2x' L_{z,j} \sin i, \\ C &= -R_{z'}^2, \end{aligned} \quad (15)$$

with $R'_{z'}$ and $D_{z'}$ from eqs (10) and (11), respectively.

The integral of the velocity profile over all allowed values of $v_{z'}$ is equal to $\Sigma_j(x', y')$. The projected velocity moments $\langle v_{z'}^n \rangle$ (with $n = 1, 2, \dots$) can be evaluated similarly, resulting in

$$\begin{aligned} \langle v_{z'} \rangle &= -C \int \frac{dz'}{R_{z'}^2} \left[J_{E_j L_{z,j}} - \frac{1}{2} B \mathcal{U}_{v_{z'}} \right]_{v_-}^{v_+} \\ \langle v_{z'}^2 \rangle &= -\frac{C}{2} \int \frac{dz'}{R_{z'}^2} \left[(v - \frac{3B}{2C}) J_{E_j L_{z,j}} + \frac{3B^2 - 4AC}{4CR_{z'}^2} \mathcal{U}_{v_{z'}} \right]_{v_-}^{v_+}, \end{aligned} \quad (16)$$

with

$$\mathcal{U}_{v_{z'}} = \arcsin \left[\frac{v_{z'} R'_{z'} + x' L_{z,j} \sin i / R'_{z'}}{\sqrt{2 E_{\text{kin}}} \sqrt{x'^2 \cos^2 i + D_{z'}^2}} \right], \quad (17)$$

and $J_{E_j L_{z,j}}$ is given in eq. (14). The values v_- and v_+ are the limits of the integration in $v_{z'}$.

2.2 Schwarzschild's method

The individual TICs can be used to model galaxies with Schwarzschild's orbit superposition method. The procedure follows the usual steps (e.g., C99). First determine the density distribution, either from a theoretical model or by deprojecting the observed projected surface density of a galaxy and choosing a mass-to-light ratio. Then calculate the corresponding gravitational potential from Poisson's equation. In this potential, define a collection of TICs by specifying the integrals $(E_j, L_{z,j})$. Jeans' theorem guarantees that a sampling of the full range in energies and angular momenta results in a TIC library that is representative for this potential. This can be achieved by sampling the radius on a grid of n_E circular radii $\{R_c\}$, chosen e.g. logarithmically on a range that includes $\geq 99.9\%$ of the mass. From this, the energy grid $\{E_c\}$ follows by calculating the energy of the circular orbit at the $\{R_c\}$. The n_{L_z} angular momenta can then be chosen linearly between the minimum ($L_z = 0$, orbits confined to the meridional plane) and maximum ($L_z = R_c v_c$, the circular orbit) at every E_c .

This choice of grids defines a library of $n_t = n_E n_{L_z}$ TICs. Schwarzschild's method then determines the weighted sum of the TICs in this library that is closest to a data set P_i (generally consisting of both photometric and kinematic data). If O_{ij} is the contribution of the j -th TIC to the i -th aperture, the problem reduces to solving for the weights γ_j in

$$\sum_j^{N_t} \gamma_j O_{ij} = P_i, \quad i = 1, \dots, N_p, \quad (18)$$

where N_p is the number of apertures for which observations

are available. The γ_j , which determine the weight of each individual TIC in this superposition, are found by using a least-squares method, with the additional constraint that $\gamma_j \geq 0$ (e.g., R97). Furthermore, $\gamma = \gamma(E, L_z)$, since every TIC is labeled by a unique combination of E and L_z . The DF that corresponds to this set of weights can then be found from (Vandervoort 1984)

$$\text{DF}(E, L_z) = \frac{\gamma(E, L_z)}{m_{E, L_z} A_{E, L_z}}, \quad (19)$$

where m_{E, L_z} is the mass of the TIC and A_{E, L_z} is the area of the cell around E and L_z in integral space.

Since the matrix problem of eq. (18) is often ill-conditioned, the weights and therefore the reconstructed DF may vary rapidly as a function of E and L_z . This can be avoided by adding regularisation constraints to the problem (e.g., Zhao 1996; R97). These constraints force the weights $\gamma(E, L_z)$ towards a smooth function of E and L_z by minimizing the n -th order derivatives $\partial^n \gamma(E, L_z) / \partial E^n, \partial^n \gamma(E, L_z) / \partial L_z^n$. The degree of smoothening is determined by the order n and by the maximum value that the derivatives are allowed to have.

The predicted observables that are obtained by calculating the weighted sum of the TICs usually differ from the observed values P_i . There are various reasons for this: the DF of the galaxy may not be of the form $f(E, L_z)$, model parameters such as inclination, stellar mass-to-light ratio or central black hole mass may not be chosen properly, the observations can contain systematical errors, and the calculations are done on finite grids, which introduces discretization effects. To measure the discrepancy, we define a quality-of-fit parameter, χ^2 , as

$$\chi^2 = \sum_{i=1}^{N_p} \left(\frac{P_i^* - P_i}{\Delta P_i} \right)^2, \quad (20)$$

in which P_i^* is the model prediction at the i -th aperture and ΔP_i is the (observational) uncertainty that is associated with P_i .

3 NUMERICAL IMPLEMENTATION

The numerical implementation of Schwarzschild's method for three-integral axisymmetric models including kinematic constraints is described in detail in C99. Here we discuss the simplifications for models containing TICs, which can be used to speed up the calculations. Readers who are more interested in applications, can skip to §4.

3.1 Storage grids

All observables are calculated on grids that are adapted to the size of the galaxy and to the constraints that have to be reproduced. The meridional plane density is stored on a polar grid in the meridional plane, with a radial grid that is sampled logarithmically on the same range as the $\{R_c\}$ and a linear grid in polar angle between 0 and $\pi/2$. The projected density is calculated on a Cartesian grid in the sky plane, and the velocity profile is stored on a three-dimensional Cartesian grid in x', y' and $v_{z'}$. The bin sizes of both grids are adapted to the resolution of the kinematic

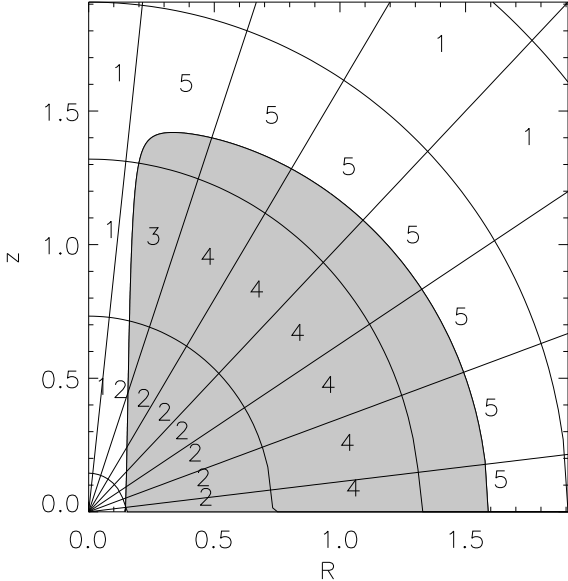


Figure 3. A ZVC($E_j, L_{z,j}$) in the meridional plane (the grey region), together with the cells of the meridional plane grid in radius and angle. The labels denote the method of integration (analytical or numerical, see text).

data to be reproduced. The observables are averaged over these grids, so that a continuous observable $O_j(\vec{x}, \vec{v})$ is represented by a discrete set of averaged grid entries

$$\langle O_j \rangle = \int_{\text{cell}} O_j(\vec{x}, \vec{v}). \quad (21)$$

All observables are related to the DF through triple (intrinsic density and velocity profile) or quadruple (projected density) integrals, two of which are trivial for TICs, because of their δ -function behaviour. This means that the averages $\langle O_j \rangle$ can be written as no worse than quadruple integrals over the region enclosed by the cross-section of the ZVC and the grid cell. Depending on the relative position of the grid cell and the ZVC, the four integrals can be interchanged and the expressions can be simplified. In the following, we show how this is achieved for all observables.

3.2 Meridional plane density

The simple form of the meridional plane density (4) leads to considerable simplifications in the evaluation of the averaged meridional plane density $\langle \rho_j \rangle$. The contribution of a general grid cell bordered by (r_-, r_+) and (θ_-, θ_+) is

$$\langle \rho_j \rangle = 2\pi^2 C \int_{r_-}^{r_+} dr \int_{\theta_-}^{\theta_+} d\theta \frac{r^2 \sin \theta}{R}. \quad (22)$$

For cells that are completely surrounded by the ZVC, which are relatively numerous for TICs with small energies (corresponding to large ZVCs), this integral can be evaluated and is given by

$$\langle \rho_j \rangle = \pi^2 C (r_+^2 - r_-^2) (\theta_+ - \theta_-). \quad (23)$$

When, on the other hand, E_j is large, so that the ZVC is less extended, the cell is (much) larger than the ZVC. This means

Cell	$r_- \in$	$r_+ \in$	$\theta_- \in$	Eq.	New range
1	$[0, R_1]$	$[0, R_1]$	-	0	-
2	$[0, R_1]$	$[R_1, R_2]$	-	22	$[R_1, r_+]$
*	$[0, R_1]$	$[R_2, \infty)$	-	22	$[R_1, R_2]$
3	$[R_1, R_2]$	$[R_1, R_2]$	$[0, \theta_{\text{ZVC}}]$	22	$[r_-, r_+]$
4	$[R_1, R_2]$	$[R_1, R_2]$	$[\theta_{\text{ZVC}}, \frac{1}{2}\pi]$	23	-
5	$[R_1, R_2]$	$[R_2, \infty)$	-	22	$[r_-, R_2]$

Table 1. For each cell in Fig. 3 (and for one cell that is not shown, labeled with *), the simplifications in the calculation of the averaged meridional plane density are given. The equation that has to be used is listed, or a value of 0 when the cell is located outside the ZVC. When eq. (22) applies, the new integration limits are given.

that the integration region in eq. (22) can be adjusted to match the ZVC size better, which speeds up the calculations considerably. Table 1 and Fig. 3 show for which cells one can apply these two simplifications. Calculating all meridional plane densities for a library of 70 x 20 TICs takes a few minutes on a machine with a 1 GHz processor.

3.3 Projected density

The average of the projected density (9) over a cell in a Cartesian grid on the sky, bordered by (x_-, x_+) and (y_-, y_+) , is given by (cf. eqs 8 and 9)

$$\langle \Sigma_j \rangle = \langle \Sigma_{z'_4} \rangle - \langle \Sigma_{z'_3} \rangle + \langle \Sigma_{z'_2} \rangle - \langle \Sigma_{z'_1} \rangle, \quad (24)$$

with

$$\langle \Sigma_{z'_k} \rangle = \frac{\pi C}{\sin i} \int_{x'_-}^{x'_+} dx' \int_{y'_-}^{y'_+} dy' \ln \left[2 \sin i \left(R'_{z'_k} + D_{z'_k} \right) \right], \quad (25)$$

(or, when $i = 0$, the integral over eq. (12)). Since $z'_k = z'_k(x', y')$, this expression cannot be simplified further without knowledge of the relation between z'_k and x', y' . Unfortunately, this relation is usually complicated and results in a very lengthy integrand, which rules out analytical evaluation. Therefore, we integrate eq. (25) numerically by using a routine for more-dimensional numerical quadrature from the NAG-library, D01FCF. These calculations are slightly more time-consuming than the ones for the meridional plane density: calculating the averaged projected densities for a library of 1400 TICs on the machine mentioned in §3.2 takes of the order of thirty minutes.

3.4 Velocity Profile

The averaged \mathcal{L} in a cell bordered by (x_-, x_+) , (y_-, y_+) and (v_-, v_+) equals

$$\langle \mathcal{L} \rangle = C \int_{x'_-}^{x'_+} dx' \int_{y'_-}^{y'_+} dy' \int_{v_-}^{v_+} dv_{z'} \int_{z'(v)_-}^{z'(v)_+} dz' J_{E_j, L_{z,j}}. \quad (26)$$

This integral is only defined on the region where the Jacobian exists, which is bordered by the points for which

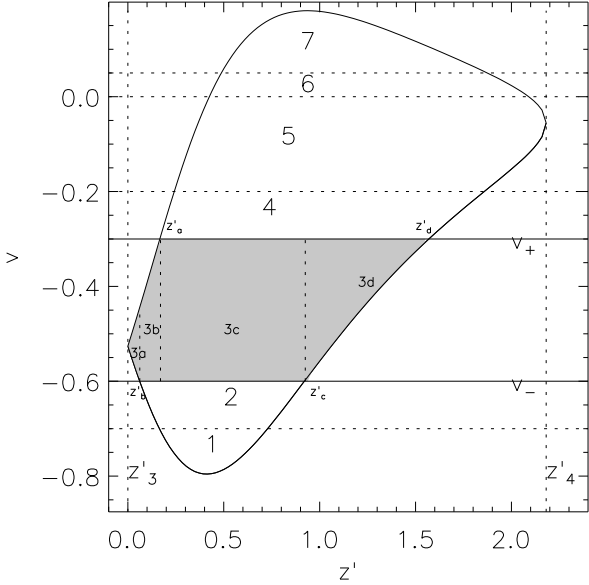


Figure 4. The extreme velocities $v_{1,2}$ of the velocity profile as a function of the line-of-sight coordinate z' , at fixed and nonzero x' and y' . Only positive values of z' are drawn, a similar configuration exists for $z' < 0$. The lower curve is v_1 , and the upper curve is v_2 . The horizontal dotted lines illustrate possible locations of the velocity bin (v_-, v_+) . The domain of integration in v and z' is the region enclosed by the curve and these bins (the grey area is an example; the new integration limits, z'_a, z'_b, z'_c, z'_d are indicated).

$A + B v_{z'} + C v_{z'}^2 = 0$ (14). We solve this equation for $v_{z'}$ to find the following relation between the minimum and maximum velocities of the velocity profile, v_1, v_2 , and z' :

$$v_{1,2}(z') = \frac{-x' L_{z,j} \sin i \pm R'_{z'} \sqrt{2 E_{\text{kin}}} \sqrt{x'^2 \cos^2 i + D_{z'}^2}}{R_{z'}^2}, \quad (27)$$

with $R'_{z'}$ and $D_{z'}$ given in eqs (10) and (11), respectively. The solid curve in Fig. 4 shows these extreme velocities as a function of z' , for arbitrary x' and y' . From eq. (27), the $v_{1,2}$ are directly proportional to E_{kin} , which means they only exist inside the intervals $[z'_1, z'_2]$ and $[z'_3, z'_4]$. When $z' = z'_i$, $E_{\text{kin}} = 0$, and the cut-off velocities are

$$\hat{v}_{1,2}(z') = -\frac{x' L_{z,j} \sin i}{R_{z'}^2}, \quad (28)$$

where \hat{v}_1 is the velocity at $z' = z'_2, z'_3$ and \hat{v}_2 is reached when $z' = z'_1, z'_4$. It follows that $v_1 = -v_2$ at $x' = 0$, so that \mathcal{L} is symmetric around $v = 0$.

Since v is integrated over the interval v_-, v_+ , the limits of integration in the inner integral of eq. (26), $z'(v)_-, z'(v)_+$, are determined by the cross-section of the velocity bin and the region enclosed by v_1 and v_2 (the grey area in Fig. 4 is an example). The z' -integration cannot in general be carried out analytically. However, we can interchange the inner two integrals and, by using the quadratic dependence of the Jacobian on $v_{z'}$, evaluate the integration over $v_{z'}$:

$$\langle \mathcal{L} \rangle_{z'_-, z'_+, v_-, v_+} = C \int_{x'_-}^{x'_+} dx' \int_{y'_-}^{y'_+} dy' \int_{z'_-}^{z'_+} dz' \frac{(\mathcal{U}_{v_+} - \mathcal{U}_{v_-})}{R'_{z'}}, \quad (29)$$

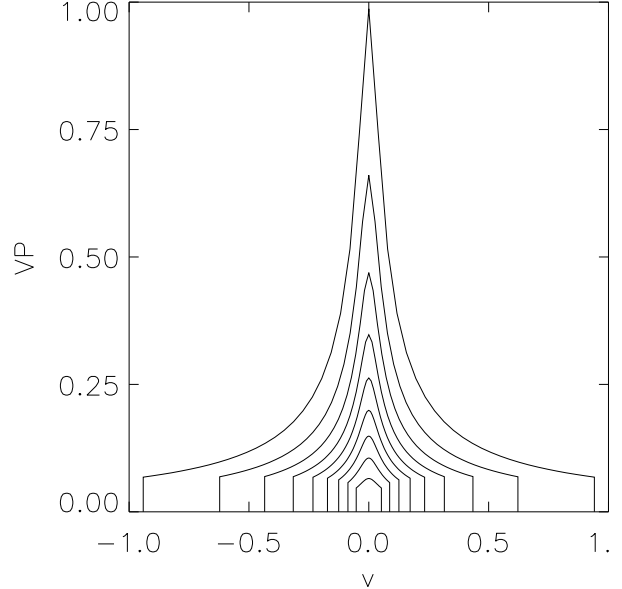


Figure 5. A series of velocity profiles along the minor axis, for a double power law density distribution (34). The formalism that is outlined in the text is used to calculate \mathcal{L} , but no average is made over the grid cells in x' and y' and very narrow bins in velocity are used to ensure that the resulting curve is smooth.

where we have used eq. (17). This expression can be simplified even further, since for the values of z' where the bin extends outside the region enclosed by v_1 and v_2 ($v_+ > v_2$, $v_- < v_1$), we can replace $v_{-,+}$ with $v_{1,2}$. In this case, we substitute eq. (27) in eq. (29), carry out the integration over z' and use eq. (25). The averaged velocity profile then equals

$$\langle \mathcal{L} \rangle_{z'_-, z'_+, v_1, v_2} = \langle \Sigma_{z'_+} \rangle - \langle \Sigma_{z'_-} \rangle. \quad (30)$$

By calculating the intersections (if any) of v_- and v_+ with $v_{1,2}$ (respectively, $z'_b < z'_c$ and $z'_a < z'_d$), we separate the integration interval in z' in regions where we use eq. (30) and others where eq. (29) applies. The averaged velocity profile in the grey area of Fig. 4 therefore consists of the averaged \mathcal{L} in the areas $\{z'_3, z'_b\} \times \{v_1(z'), v_2(z')\}$ (area 3a), $\{z'_b, z'_a\} \times \{v_-, v_2(z')\}$ (area 3b), $\{z'_a, z'_c\} \times \{v_-, v_+\}$ (area 3c), and $\{z'_c, z'_d\} \times \{v_1(z'), v_+\}$ (area 3d), which contribute, respectively, $\langle \mathcal{L} \rangle_{z'_3, z'_b, v_1, v_2}$, $\langle \mathcal{L} \rangle_{z'_b, z'_a, v_-, v_2}$, $\langle \mathcal{L} \rangle_{z'_a, z'_c, v_-, v_+}$ and $\langle \mathcal{L} \rangle_{z'_c, z'_d, v_1, v_+}$. The total averaged velocity profile in this cell is then given by the sum of these four terms. A similar reasoning applies to all other bins in Fig. 4 (Table 2). To check whether the resulting \mathcal{L} is smooth and resembles those calculated by C99, we have calculated a series of \mathcal{L} 's along the minor axis (which means they are symmetric around $v = 0$). The result is shown in Fig. 5, which can be compared to, e.g., Fig. 5 of C99.

3.5 PSF convolution

In the previous subsections, we described how to obtain the average of the TIC observables over the cells of the storage grids. These quantities can only be compared with observational data when point spread function (PSF) effects are taken into account correctly. This means that observationally accessible quantities such as the projected density and

Cell	$v_- \in$	$v_+ \in$	$z', v_{z'} \in$
1	$(-\infty, \hat{v}_1]$	$(-\infty, \hat{v}_1]$	$\{z'_a, z'_d\} \times \{v_1, v_+\}$
2	$(-\infty, \hat{v}_1]$	$(-\infty, \hat{v}_1]$	$\{z'_a, z'_b\} \times \{v_1, v_+\}$ $\{z'_b, z'_c\} \times \{v_-, v_+\}$ $\{z'_c, z'_d\} \times \{v_1, v_+\}$
3	$(-\infty, \hat{v}_1]$	$[\hat{v}_1, \hat{v}_2]$	$\{z'_3, z'_b\} \times \{v_1, v_2\}$ $\{z'_b, z'_c\} \times \{v_-, v_2\}$ $\{z'_a, z'_c\} \times \{v_-, v_+\}$ $\{z'_c, z'_d\} \times \{v_1, v_+\}$
*	$(-\infty, \hat{v}_1]$	$[\hat{v}_2, \infty)$	$\{z'_3, z'_d\} \times \{v_1, v_2\}$
4	$[\hat{v}_1, \hat{v}_2]$	$[\hat{v}_1, \hat{v}_2]$	$\{z'_b, z'_a\} \times \{v_-, v_2\}$ $\{z'_a, z'_c\} \times \{v_-, v_+\}$ $\{z'_c, z'_d\} \times \{v_1, v_+\}$
5	$[\hat{v}_1, \hat{v}_2]$	$[\hat{v}_2, \infty)$	$\{z'_d, z'_b\} \times \{v_1, v_2\}$ $\{z'_b, z'_a\} \times \{v_-, v_2\}$ $\{z'_a, z'_d\} \times \{v_-, v_+\}$ $\{z'_d, z'_1\} \times \{v_1, v_+\}$
6	$[\hat{v}_2, \infty)$	$[\hat{v}_2, \infty)$	$\{z'_b, z'_a\} \times \{v_-, v_2\}$ $\{z'_a, z'_1\} \times \{v_-, v_+\}$ $\{z'_b, z'_d\} \times \{v_-, v_2\}$
7	$[\hat{v}_2, \infty)$	$[\hat{v}_2, \infty)$	$\{z'_a, z'_d\} \times \{v_-, v_2\}$

Table 2. The first column gives the label of the velocity bins in Fig. 4 (and for one bin that is not shown, denoted with *). The second and third column give the intervals in which the limits of the velocity bin, v_- and v_+ , are located. In the fourth column, the domains in $(z', v_{z'})$ on which eq. (29) and eq. (30) are defined, are given. The total velocity profile is then obtained by adding the contributions of all these regions.

the velocity profile have to be convolved with the appropriate PSF, which is usually described in terms of a (sum of) Gaussian functions. The extra two-dimensional integration that this convolution introduces can be carried out analytically when it is combined with the average over the storage cell (see Appendix D of Q95). This means that an extra term, consisting of error functions, appears in the expressions for the observables that were given previously.

4 EXAMPLES AND TESTS

To test our method, we apply the numerical implementation to three theoretical potential-density pairs. We investigate whether our formalism rules out the same models as previous methods and determine the accuracy with which a theoretical distribution function can be reproduced. This also allows us to study the behaviour of the χ^2 (20) and the regularisation algorithm, which is similar to the one that is used in the three-integral Schwarzschild methods (C99). Applications to two-dimensional photometry and kinematics of galaxies are described in Verolme et al. and McDermid et al.

4.1 Regularisation: Kuzmin-Kutuzov model

We first test the ability of our method to reproduce a known $f(E, L_z)$, given ρ and V , and investigate the effect of regularisation on the results. We use the density and potential of the Kuzmin-Kutuzov (1962) model

$$\rho(R, z) = \frac{M c^2}{4 \pi} \frac{(a^2 + c^2) R^2 + 2 a^2 (z^2 + c^2) + a^4 + 3 a^2 u}{u^3 (R^2 + z^2 + a^2 + c^2 + 2 u)^3},$$

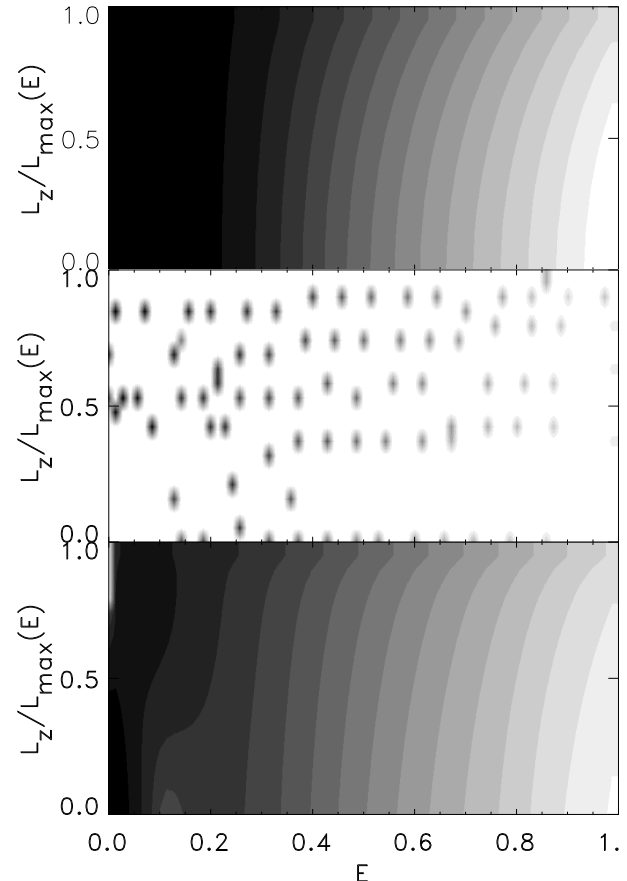


Figure 6. The upper panel shows the Kuzmin-Kutuzov DF (32) as a function of energy E and fractional angular momentum $L_z/L_{z,\max}$. The contour levels are chosen logarithmically and darker shading corresponds to larger values of the DF. The reconstructed DF (19) for a two-integral Schwarzschild model that fits only the meridional plane masses is shown in the middle panel. There is a large discrepancy between the two functions. The lower panel shows the smooth DF that is found by including regularisation constraints in the fit. The contours are drawn at the same levels as in the top panel, showing that this DF reproduces the theoretical model very closely. The fractional difference between the two DFs on a range that includes $> 99\%$ of the mass is smaller than 10^{-3} .

$$V(R, z) = \frac{G M}{\sqrt{R^2 + z^2 + a^2 + c^2 + 2u}}, \quad (31)$$

with $u = \sqrt{c^2 R^2 + a^2 (z^2 + c^2)}$. The density distribution is nearly spheroidal, and many of the properties of these models, including the projected surface density, can be evaluated explicitly.

The even part of the $f(E, L_z)$ distribution function for the Kuzmin-Kutuzov models is given by (Dejonghe & de Zeeuw 1988; Batsleer & Dejonghe 1993)

$$f(E, L_z) = \frac{c^2 E^{5/2}}{\sqrt{8a\pi^3}} \sum_{\epsilon=-1,1} \int_0^1 dt \frac{(1-t^2) \left[(3+4x_\epsilon - x_\epsilon^2)(1-x_\epsilon)(1-t^2) + 12t^2 \right]}{(1-2aE t \sqrt{1-t^2} + \epsilon L_z t \sqrt{2hE})^5}, \quad (32)$$

with

$$x_\epsilon(t) = 2aE t \frac{\sqrt{1-t^2}}{1+\epsilon\sqrt{z}t}. \quad (33)$$

This integral can be expressed in terms of elementary functions, but this leads to an exceedingly lengthy expression, and it is best evaluated numerically. A grey-scale plot of the Kuzmin-Kutuzov DF as a function of energy and fractional angular momentum is shown in the upper panel of Fig. 6.

We attempted to reproduce this DF by calculating a two-integral Schwarzschild model that fits the meridional plane mass (31). We used $n_E = 70$ and $n_{L_z} = 20$, including $L_z = 0$, and adopted 16 radial and 7 angular bins, like C99. With these parameters, the model density was fitted with very high accuracy (fractional difference smaller than 0.001), but the TIC weights vary dramatically with energy and angular momentum, resulting in a very jagged DF (the middle panel in Fig. 6). Including regularisation constraints enforces the weights to vary smoothly with TIC index, resulting in a DF that reproduces the theoretical DF to within 0.1%. This is illustrated in the lower panel of Fig. 6, which was obtained by requiring the same fitting accuracy (ΔP in eq. 20) for both the meridional plane masses and the regularisation constraints. This means that both constraint types have equal influence on the final model, so that the model DF is smooth, but still reproduces the density.

In order to measure how fitting to the mass determines the kinematics of the model, we have calculated a theoretical velocity profile on the minor axis directly from the distribution function eq. (19), and compared this with the predicted profile, given by the superposition of all the individual TIC velocity profiles. Fig. 7 demonstrates that the agreement between the two curves is significantly better than the typical measurement error in observed velocity profiles (van der Marel & Franx 1993; Joseph et al. 2001).

4.2 Models with a central black hole

We now consider $f(E, L_z)$ models with a central black hole, represented by a point mass with potential GM_\bullet/r .

For spherically symmetric galaxies, there is a direct relation between the luminous density distribution and the isotropic distribution function $f(E)$ (Eddington 1916). When the DF is required to be non-negative, this relation implies that no spherical, isotropic galaxies with a central black hole exist for cusp slopes shallower than -0.5 (e.g., Binney & Tremaine 1987). An indication that this restriction disappears when a higher degree of anisotropy is allowed is illustrated by the $f(E, L^2)$ (with L the angular momentum) that is obtained by placing all stars on circular orbits (Hunter 1975a).

To investigate this effect for general anisotropic distribution functions $f(E, L_z)$, Q95 applied the HQ-method to density distributions that are stratified on similar concentric spheroids. They considered models with a density profile that follows a double power law, given by

$$\rho = \rho_0 \left(\frac{m}{b}\right)^\alpha \left[1 + \left(\frac{m}{b}\right)^2\right]^\beta, \quad (34)$$

where ρ_0 and α are the central density and cusp slope, $m^2 = R^2 + z^2/q^2$ with q the intrinsic axis ratio, and b is the break

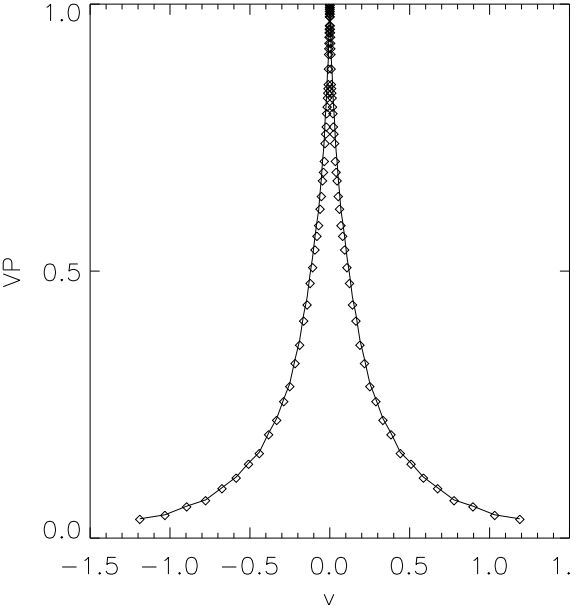


Figure 7. The theoretical velocity profile for a point on the minor axis, calculated directly from eq. (19) (the solid line), and the superposition of all individual TIC velocity profiles (indicated with diamonds) for the Kuzmin-Kutuzov density distribution of eq. (31). The two curves agree to 0.1%.

radius. Q95 found that all oblate ($q < 1$) double power law profiles correspond to a non-negative distribution function. However, adding a central black to these models limits the central cusp slope to $\alpha < -0.5$, as in the spherical case. This restriction is independent of black hole mass, as long as $M_\bullet > 0$.

De Bruijne et al. (1996) showed that this result is valid for a much larger family of cusped spheroidal density profiles with a central black hole: when the potential is spherically symmetric, the distribution function

$$f(E, L^2, L_z) = \sum_{\mu, \lambda} \left(\frac{L}{L_{\max}}\right)^\mu \left(\frac{L_z}{L_{\max}}\right)^\lambda g(E), \quad (35)$$

corresponds to the density

$$\rho(r, \theta) = \sum_{\mu, \lambda} D^{\mu, \lambda} r^{-\alpha} \sin^{2\lambda} \theta, \quad (36)$$

in which the $D^{\mu, \lambda}$ are given in terms of Γ -functions by eq. (17) of de Bruijne et al. The argument of a Γ -function must be positive, which implies that, near a black hole, where the potential falls off as $1/r$ ($\delta = 1$ in their notation), eqs (35) and (36) exist only for

$$\alpha < \lambda - \mu - \frac{1}{2}. \quad (37)$$

We see from eq. (35) that the limiting case of a two-integral DF $f(E, L_z)$ is given by $\mu = 0$, so that eq. (37) reduces to

$$\alpha < \lambda - \frac{1}{2}. \quad (38)$$

This means that density distributions that can be expanded in terms of $\sin \theta$ must obey condition (38) on each of the terms of the expansion in order to have a physical DF near the black hole. The lowest-order term of this expansion, usually with $\lambda = 0$, places the most stringent condition on α , i.e. $\alpha < -0.5$.

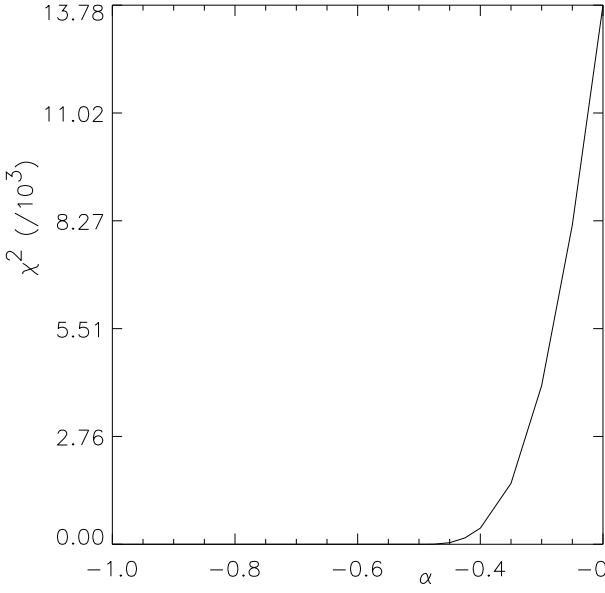


Figure 8. The quality-of-fit χ^2 for selfconsistent two-integral models as a function of cusp slope α , at constant intrinsic flattening. The χ^2 is large for values in the interval $[-0.5, 0]$, and negligible for $\alpha < -0.5$. This is caused by the non-existence of the self-consistent $f(E, L_z)$ models with $\alpha > -0.5$.

These results show that analytical methods are very powerful for deriving criteria for the existence of models. In contrast, Schwarzschild's method always finds an orbit superposition that fits the constraints to some degree. The χ^2 (20), determined from residual errors, is the only measure for the existence of the underlying distribution function. A priori, it is not clear whether this parameter is able to reproduce the sharp limits on the model parameters that are found with analytical methods. For this reason, we constructed two-integral models for the density profile (34). We added a central point mass $M_\bullet \sim 1\%$ of the total galaxy mass, mimicking a central black hole, and varied the cusp slope at constant flattening. As in §4.1, we took $n_E = 70$ and $n_{L_z} = 20$ (again including $L_z = 0$), and adopted 16 radial and 7 angular bins.

Fig. 8 shows the resulting χ^2 as function of α for self-consistent two-integral models. While $\chi^2 < 10^{-5}$ for values of α below -0.5 , it increases rapidly as soon as α increases above -0.5 . This shows that our method recovers the models of Q95, and that our goodness-of-fit parameter χ^2 is a good discriminator of the (non)-existence of a given model.

We also investigated the axisymmetric version of the triaxial models with central cusps that were introduced by de Zeeuw & Carollo (1996). The potential and density are given in Appendix A. The behaviour of these models is completely determined by their axis ratios at small and large radii, q_0 and q_∞ , and the central cusp slope α . The density distribution is dimpled on the symmetry axis, and, for some choices of α, q_0 , even becomes negative. In advance, we can therefore rule out a (small) range of parameters for which the DF does not exist. The physical range of q_0 decreases when q_∞ is decreased. At $q_\infty = 0.99$, which is considered here, models with $q_0 < 0.05$ show this behaviour. We study the range $0.1 < q_0 < 1$.

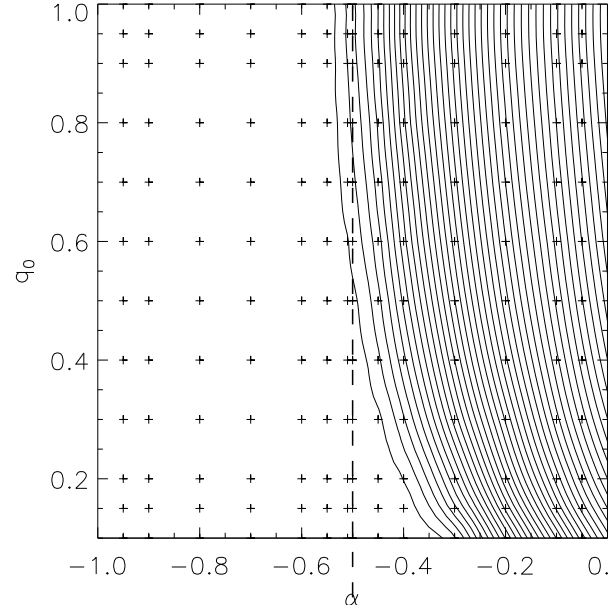


Figure 9. The quality of fit χ^2 as a function of central cusp slope α and intrinsic flattening q_0 , for a value of the flattening at infinity $q_\infty = 0.99$. The dashed line shows the theoretical limit on the cusp slope for two-integral distribution functions and the crosses indicate combinations of α and q_0 for which models were calculated.

We added a central black hole with a mass $\sim 1\%$ of the total mass, and calculated self-consistent two-integral models using the same grid settings as in §4.1. Fig. 9 shows the contours of constant χ^2 as a function of α and q_0 . As expected, the χ^2 is zero for values $\alpha < -0.5$ and rises rapidly above $\alpha = -0.5$, indicating that self-consistent two-integral distribution functions do not exist at these values of the central cusp slope. However, for $q_0 < 0.4$, the transition to $\chi^2 > 0$ occurs at values of $\alpha > -0.5$, which means that these flatter models have an even larger freedom in possible central cusp slopes. The points that contribute most to this nonzero χ^2 are located in the center of the model, i.e., near the black hole, and experiments with a denser sampling in the integrals of motion give similar results. The limiting behavior of the density is (cf. eq (A3)

$$\lim_{r \rightarrow 0} \rho(r, \theta) = \frac{3}{2} g(r) \left[\frac{1}{q_0^{q_0-1}} + \sin^2 \theta \right], \quad (39)$$

so that the importance of the constant term in the expansion (36) decreases when q_0 decreases. This may gradually relax the restriction on α in the numerical model. A similar effect has been found recently in oblate Sridhar-Touma models (Jalali & de Zeeuw 2001), which resemble the power-law models in many respects. However, the values of q_0 for which this occurs are much smaller than the observed flattenings of early-type galaxies.

5 SUMMARY AND CONCLUSIONS

We have presented an alternative to the existing analytical and numerical methods for calculating two-integral distribution functions. It is based upon Schwarzschild's orbit superposition method and able to deal with arbitrary den-

sity profiles and galaxy potentials. Instead of orbital building blocks, we use the so-called two-integral components, which are smoother and implicitly include stochastic orbits. Due to their delta-function behaviour, the observables can be calculated (semi-)analytically, which speeds up the calculations considerably. We checked that the method is able to reproduce a known combination of potential, density and distribution function and tested the regularisation algorithm in the process. This test shows that fitting the meridional plane masses alone is not enough to constrain the DF, while including a (modest) amount of regularisation is enough to smoothen the DF toward the theoretical curve.

We have also tested the χ^2 (20), which measures the quality-of-fit of the resulting model, against analytical investigations. This demonstrates that a high value of χ^2 can be taken as a sure indication that the model does not exist.

These results show that our method is flexible and reproduces analytical results very closely. Additionally, many of the characteristics of the implementation that we used, such as the regularisation method and the χ^2 -parameter, are used in more general (three-integral) models. Regularisation is therefore also a very useful and necessary tool to smoothen the distribution function that is found by these methods, and the χ^2 -parameter is a useful diagnostic to test the existence of the resulting models. Applications in which we calculate fully three-integral models (including TICs) of observed kinematics will follow in a subsequent paper.

Acknowledgements

It is a pleasure to thank Glenn van de Ven, Michele Cappellari and Roeland van der Marel for useful discussions and a critical reading of the manuscript. Furthermore, we are very thankful to Roeland van der Marel for kindly providing his three-integral Schwarzschild software.

REFERENCES

- Batsleer P., Dejonghe H., 1993, A&A, 271, 104
 Binney J.J., 1982, MNRAS, 201, 15
 Binney J.J., Tremaine S.D., 1987. Galactic Dynamics, Princeton University Press, Princeton
 Bower G.A. et al., 2001, ApJ, 550, 75
 van den Bosch F.C., de Zeeuw P.T., 1996, MNRAS, 283, 381
 de Bruijne J.H.J., van der Marel R.P., de Zeeuw P.T., 1996, MNRAS, 282, 909
 Copin Y., Zhao H.S., de Zeeuw P.T., 2000, MNRAS, 318, 781
 Cretton N. et al., 1999, ApJS, 124, 383 (C99)
 Cretton N., Rix H.W., de Zeeuw P.T., 2000, ApJ, 536, 319
 Dehnen W., Gerhard O.E., 1994, MNRAS, 268, 1019
 Dejonghe H., 1986, Phys. Rep. 133, 218
 Dejonghe H., de Zeeuw P.T., 1988, ApJ, 333, 90
 Eddington A.S., 1916, MNRAS, 76, 572
 Gebhardt K., et al., 2000, AJ, 119, 115
 Häfner R., et al., 2000, MNRAS, 314, 433
 Hunter C., 1975a, IAUS 69, 195H
 Hunter C., 1975b, AJ, 80, 783
 Hunter C., Qian E.E., 1993, MNRAS, 262, 401
 Jalali M.A. & de Zeeuw, P.T., MNRAS, submitted
 Joseph C.L. et al., 2001, ApJ, 550, 668
 Kuijken K., 1995, ApJ, 446, 194
 Kuzmin G.G., 1956, Astr. Zh., 33, 27
 Kuzmin G.G., Kutuzov, S.A., 1962, Bull. Abast. Ap. Obs., 27, 82
 Lake G., 1981, ApJ, 243, 111
 Lauer T., et al., 1995, AJ, 110, 2622
 Levison H.F., Richstone D., 1985, ApJ, 295, 340
 Lynden-Bell D., 1962, MNRAS, 123, 447
 van der Marel R.P., 1991, MNRAS, 253, 710
 van der Marel R.P. & Franx M., 1993, ApJ, 407, 525
 van der Marel R.P. et al., 1994, MNRAS, 271, 99
 van der Marel R.P. et al., 1998, ApJ, 493, 613 (vdM98)
 Magorrian J., 1995, MNRAS, 277, 1185
 Magorrian J. et al., 1998, AJ, 115, 2285
 Merritt D.R., Fridman T., 1996, ApJ, 460, 136
 Pfenniger D., 1984, A&A, 141, 171
 Qian E.E., et al., 1995, MNRAS, 274, 602 (Q95)
 Richstone D., Tremaine S., 1984, ApJ, 286, 27
 Rix H.-W., et al., 1997, ApJ, 232, 236 (R97)
 Schwarzschild M., 1979, ApJ, 232, 239
 Schwarzschild M., 1982, ApJ, 263, 000
 Schwarzschild M., 1993, ApJ, 409, 563
 Shaw M., et al., A&A, 268, 511
 Siopis C., Kandrup H. E., 2000, MNRAS, 319, 43
 Statler, T.S., 1987, ApJ, 321, 113
 Vietri M., 1986, ApJ, 306, 48
 de Zeeuw P.T., 1985, MNRAS, 216, 273
 de Zeeuw P.T., Carollo C.M., 1996, MNRAS, 281, 1333
 Zhao H.S., 1996, MNRAS, 283, 149

APPENDIX A: A FAMILY OF AXISYMMETRIC MODELS

The axisymmetric limit of the triaxial models introduced by de Zeeuw & Carollo (1996) is defined by the potential

$$V(r, \theta) = -u(r) + \frac{1}{2}(3 \cos^2 \theta - 1)v(r), \quad (\text{A1})$$

with

$$\begin{aligned} u(r) &= \begin{cases} \ln \frac{r}{r+1} & \text{for } \alpha = -2 \\ \frac{1}{2+\alpha} \left[\left(\frac{r}{r+1} \right)^{2+\alpha} - 1 \right] & \text{for } \alpha \neq -2 \end{cases} \\ v(r) &= -\frac{Ar^{2+\alpha}}{(r+r_2)^{4+\alpha}}, \end{aligned} \quad (\text{A2})$$

where A and r_2 are constants, we have chosen $GM = 1$, and consider $\alpha \geq -3$. The corresponding density distribution is

$$\rho(r, \theta) = g(r) \left[\frac{f(r)}{g(r)} - 1 + \frac{3}{2} \sin^2 \theta \right] \quad (\text{A3})$$

with

$$\begin{aligned} f(r) &= \frac{(3+\alpha)r^\alpha}{4\pi(r+1)^{4+\alpha}} \\ g(r) &= \frac{Ar^\alpha [4r^2 + 4(6+\alpha)r r_2 - \alpha(5+\alpha)r_2^2]}{4\pi(r+r_2)^{6+\alpha}}. \end{aligned} \quad (\text{A4})$$

The constants A and r_2 are related to the axis ratios of the density distribution at small and large radii, q_0 and q_∞ , respectively, by

$$\begin{aligned} A &= \frac{(3+\alpha)(1-q_\infty^4)}{2(2+q_\infty^4)} \\ r_2 &= \left[\frac{-(1-q_\infty^4)(2+q_0^{-\alpha})\alpha(5+\alpha)}{4(1-q_0^{-\alpha})(2+q_\infty^4)} \right]^{1/(4+\alpha)}, \end{aligned} \quad (\text{A5})$$

This paper has been produced using the Royal Astronomical Society/Blackwell Science L^AT_EX style file.